

Contents

2	1	Charge monitoring	2
3		<i>The ATLAS Diamond Beam Monitor</i>	2
4	1.1	Luminosity measurements	3
5	1.2	Diamond pixel module	4
6	1.2.1	Sensors	4
7	1.2.2	Front-end electronics	5
8	1.3	Module assembly	8
9	1.4	Performance results	8
10	1.4.1	Source test results	8
11	1.4.2	Erratic current	12
12	1.4.3	Test beam results	12
13	1.4.4	Summary of the QC	13
14	1.5	Installation and commissioning	13
15	1.5.1	Positioning in ATLAS	15
16	1.6	Operation	16
17	1.7	Conclusion	18

¹⁸ **Chapter 1**

¹⁹ **Charge monitoring**

²⁰ *The ATLAS Diamond Beam Monitor*

²¹ Particle detectors in high energy physics experiments need to meet very stringent
²² specifications, depending on the functionality and their position in the experiment.
²³ In particular, the detectors close to the collision point are subject to high levels
²⁴ of radiation. In addition, they need to operate with a high spatial and temporal
²⁵ segmentation to be able to precisely measure trajectories of hundreds of particles
²⁶ in very short time. In addition, they need to be highly efficient. In terms of the
²⁷ structure, their active sensing material has to be thin so as not to cause the particles
²⁸ to scatter or get stopped, which would worsen the measurements. This also means
²⁹ that they have to have a low heat dissipation so that the cooling system dimensions
³⁰ can be minimised. Finally, they need to be able to have a stable operation for several
³¹ years without a required intervention, because they are buried deep under tonnes of
³² material and electronics.

³³ The material of choice for the inner detector layers in the HEP experiments is
³⁴ silicon. It can withstand high doses of radiation, it is highly efficient (of the order
³⁵ of $\sim 99.9\%$) and relatively low cost due to using existing industrial processes for its
³⁶ production. Its downside is that, with increasing irradiation levels, it needs to be
³⁷ cooled to increasingly low temperatures to ensure a stable operation. This is not the
³⁸ case with diamond. In addition, diamond has a lower radiation damage factor, which
³⁹ means it can operate in a radiation-heavy environment for a longer period.

⁴⁰ The ATLAS Diamond Beam Monitor (the DBM) [10] is a novel high energy
⁴¹ charged particle detector. Its function is to measure luminosity and beam background
⁴² in the ATLAS experiment. Given its position in a region with a high radiation dose,
⁴³ diamond was chosen as the sensing material. The monitor's pCVD diamond sensors
⁴⁴ are instrumented with pixellated FE-I4 front-end chips. The pCVD diamond sensor
⁴⁵ material was chosen to ensure the durability of the sensors in a radiation-hard envi-
⁴⁶ ronment and the size of its active area. The DBM is not the first diamond detector
⁴⁷ used in HEP, but it is the largest pixellated detector installed thus far, as shown in
⁴⁸ figure 1.1. It was designed as an upgrade to the existing luminosity monitor called

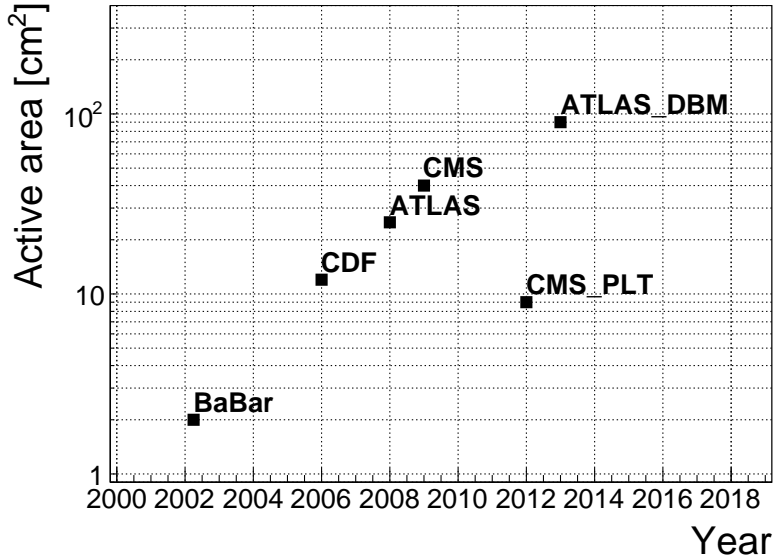


Figure 1.1: Diamond detectors installed in high-energy physics experiments in the last decade, sorted by the active sensor area. The first four detectors from the left are radiation monitors whereas the right two are pixel trackers.

the Beam Conditions Monitor (BCM) [6] consisting of eight diamond pad detectors. The BCM is able to perform precise time-of-flight (ToF) measurements. The DBM complements the BCM’s features by implementing tracking capability. Its pixelated front-end electronics significantly increase the spatial resolution of the system. Furthermore, the DBM is able to distinguish particle tracks originating in the collision region from the background hits. This capability is a result of its projective geometry pointing towards the interaction region. This chapter first describes the principles of luminosity measurements. It then explains how the DBM carries out this task. Finally, some results from the commissioning and from the real collisions are presented.

When a particle traverses a sensor plane, a hit is recorded in the corresponding pixel. Thus, a precise spatial and timing information of the hit is extracted. With three or more sensors stacked behind each other, it is also possible to define the particle’s trajectory. This is the case with the DBM. Its projective geometry allows the particles to be tracked if they traverse the sensor planes. The DBM relates the luminosity to the number of particle tracks that originate from the collision region of the ATLAS experiment. Particles that hit the DBM from other directions are rejected as background radiation.

1.1 Luminosity measurements

Luminosity is one of the most important parameters of a particle collider. It is a measurement of the rate of particle collisions that are produced by two particle beams. It can be described as a function of the beam parameters, such as: the number of

1.2. DIAMOND PIXEL MODULE

70 colliding bunch pairs, the revolution frequency, the number of particles in each bunch
71 and the transverse bunch dimensions. The first four parameters are well defined.
72 However, the transverse bunch dimensions have to be determined experimentally
73 during calibration measurements. The ATLAS experiment uses the *van der Meer*
74 *scan* [3] during low-luminosity runs to calibrate the luminosity detectors. This scan
75 is performed by displacing one beam in a given direction and measuring the rate
76 of interactions as a function of the displacement. The transverse charge density of
77 the bunches can be estimated on the basis of the interaction rate. The calibrated
78 luminosity detectors can then operate during high-luminosity runs.

79 One approach to luminosity monitoring is to count the number of particles pro-
80 duced by the collisions. The luminosity is then proportional to the number of detected
81 particles. A detector has to be capable of distinguishing individual particles that fly
82 from the interaction point through the active sensor area. If the detector has at least
83 three layers, it can reconstruct the particles' tracks, which in turn yields more infor-
84 mation on their trajectory. This is one reason why detectors with a high timing-
85 and spatial segmentation are more suitable for these applications. The second reason
86 is that, with a high spatial segmentation, the detector does not saturate even at high
87 particle fluencies.

88 1.2 Diamond pixel module

89 The two most important parts of the diamond pixel module are the sensor, which
90 translates the incident ionising radiation into charge carriers as explained in chap-
91 ter ??, and the pixellated front-end chip, which collects the ionised charge with a high
92 spatial segmentation, processes the recorded data and sends them to the readout sys-
93 tem. This section describes these two parts of the module and their interconnection.

94 1.2.1 Sensors

95 The DBM modules are instrumented with two types of sensors – pCVD diamond
96 and silicon. The silicon sensors are used as a fallback solution because there were
97 not enough high-quality diamond sensors available during the construction phase. In
98 addition, a comparative study of irradiation damage between silicon and diamond
99 can be made with such a hybrid system.

100 **Diamond sensors** The target material for this application is pCVD diamond. The
101 reason for this is that the active area of an individual sensor must be approximately
102 4 cm^2 , which is too large for the sCVD diamond. pCVD material is also a bit cheaper,
103 which makes a detector with a large active area more feasible to build. The material
104 is provided by three companies: DDL, E6 and II-IV and it is grown in 15 cm wafers,
105 as seen in figure 1.2. The target thickness of the wafers is 500 μm . The minimum
106 required charge collection efficiency is 40 % ($\text{CCD} \geq 200 \mu\text{m}$) to ensure that the
107 MPV of the collected charge for MIPs is still well above the noise of the electronics

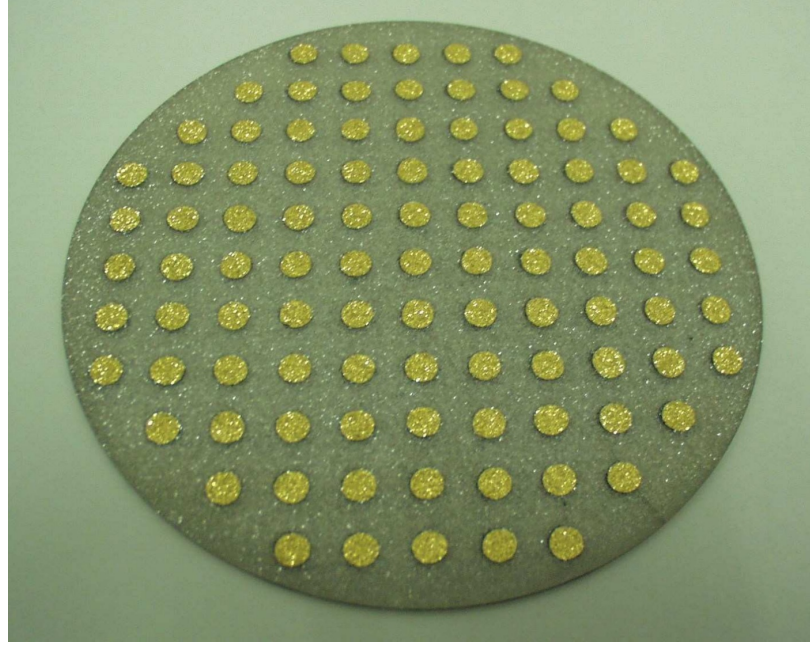


Figure 1.2: A pCVD wafer. The golden dots on the surface are the electrodes that are applied during the qualification test. The wafer is measured across the surface to find the regions with the highest efficiency.

even after heavy irradiation. They need to be operated at bias voltages between 600–1000 V. On one side there is a single gold electrode applied across the entire surface. On the other side a pixellated metallisation is added.

Silicon sensors are standard $n^+ - in - n$ planar sensors with a 200 μm thickness and were fabricated at CiS [1], a company from Erfurt, Germany. They are designed to have nearly a 100 % efficiency when not irradiated. One side is segmented into pixels. Guard rings at the edges of the sensor provide a controlled drop in potential, reducing the possibility of shorts at maximum design bias voltages of the order of 1000 V.

1.2.2 Front-end electronics

The FE-I4 (front-end version four) [4] is an ASIC pixel chip designed specifically for the ATLAS pixel detector upgrade. It is built as a successor to the current pixel chip FE-I3, surpassing it in size of the active area ($6\times$ larger) as well as the number of channels/pixels ($10\times$ more). 336 such FE-I4 modules are used in the newly installed pixel layer called the Insertable B-Layer (IBL) [7]. The DBM is also instrumented with these chips. The FE-I4's integrated circuit contains readout circuitry for 26880 pixels arranged in 80 columns on a 250 μm pitch and 336 rows on a 50 μm pitch. The size of the active area is therefore $20.0 \times 16.8 \text{ mm}^2$. This fine granularity allows for a high-precision particle tracking. The chip operates at 40 MHz with a 25 ns acquisition window, which corresponds to the spacing of the particle bunches in the LHC. It is

1.2. DIAMOND PIXEL MODULE

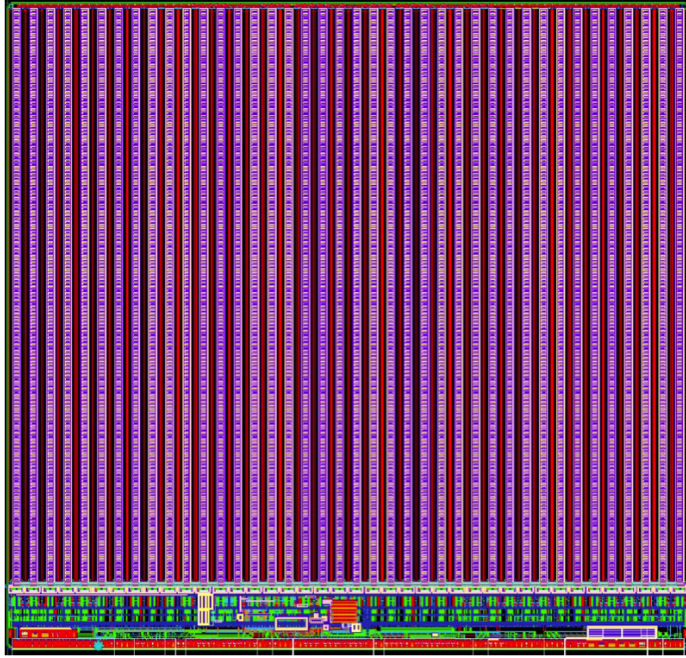


Figure 1.3: FE-I4 layout, top-down view. The pink area are pixels grouped into columns, the green area below is the common logic and the red strip at the bottom are the wire bond pads.

128 hence able to correlate hits/tracks to their corresponding bunch. Furthermore, each
129 pixel is capable of measuring the deposited charge of a detected particle by using
130 the Time-over-Threshold (ToT) method. Finally, the FEI4 has been designed to
131 withstand a radiation dose up to 300 MGy. This ensures a longterm stability in the
132 radiation hard forward region of the ATLAS experiment.

133 Each pixel is designed as a separate entity. Its electrical chain is shown in fig-
134 ure 1.4. The bump-bond pad – the connection to the outside of the chip – is the
135 input of the electrical chain, connected to a free-running amplification stage with ad-
136 justable shaping using a 4-bit register at the feedback branch. The analog amplifier is
137 designed to collect negative charge, therefore electrons. The output is routed through
138 a discriminator with an adjustable threshold. This value in effect defines the level
139 at which the circuit detects a hit. In addition, there is a counter of the clock cycles
140 (25 ns sampling) during which the signal is above the discriminator threshold. The
141 value of the counter is proportional to the collected charge. The logic gates at the
142 end of the chain are used to enable/disable the pixel and to issue a so-called HitOr
143 flag – this signal is set whenever at least one of the pixels was hit and is used as a
144 trigger for the readout. The output of the chain – HitOut – is routed into the logic
145 of the chip where it is buffered and sent out to the readout system. The module
146 receives all its commands from the system via a 40 MHz LVDS line. The commands
147 are either settings for the pixel registers or triggers that start the data readout. The
148 data are sent via an LVDS line at up to 320 Mbit/s, but by default at 160 Mbit/s,
149 four times faster than the clock of the device. This allows the chip to clear out its

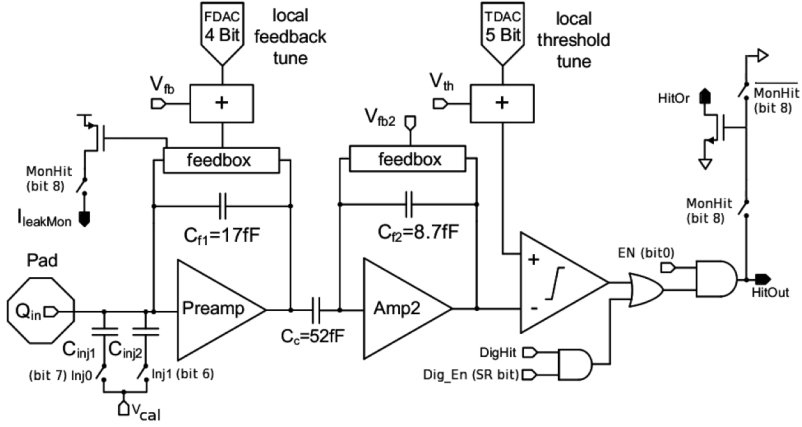


Figure 1.4: Schematic of an analog pixel. Courtesy of the FE-I4 collaboration.

150 buffers before new data are recorded, thus avoiding dead time and data pile-up. The
151 FE-I4 has been successfully tested for trigger rates of up to 300 kHz, depending on
152 the occupancy per trigger.

153 The DBM uses pCVD diamond with $d_C = 500 \mu\text{m}$ thickness and silicon with
154 $d_{Si} = 200 \mu\text{m}$ thickness as a sensor material. The resulting most probable value
155 (MPV) of the deposited charge for a minimum ionising particle (MIP) is calculated
156 with the formula $Q_S = d \cdot E_{e-h}$ and equals 18000 electrons and 17800 electrons,
157 respectively, at a full charge collection efficiency. Unfortunately this is not the case
158 with the pCVD material, whereby the expected charge collection efficiency is of the
159 order of 50 % – around 9000 e. This value further decreases with received irradiation
160 dose. Therefore in order to detect the particles depositing energy on the far left side
161 of the landau spectrum, the threshold has to be set to a significantly lower value. On
162 the other hand, if the threshold set too low, it also detects the electronic noise and
163 generates false hits. Typical noise amplitudes are in the range of 120–200 e. A safe
164 threshold range is approximately five times above this value. The target for the DBM
165 is to set the threshold to 800 e.

166 The analog amplifier is implemented in two stages to get a fast rise time at a low
167 noise and a low power consumption. The output signal of the analog amplifier has a
168 triangular shape with a fast rise time and a long decay. The shape can be adjusted by
169 tuning the amplifier feedback loop. Its length is proportional to the collected charge,
170 but it needs to be calibrated first. This is done by means of two injection capacitors,
171 C_{inj1} and C_{inj2} , seen in figure 1.4 with well defined capacitances. First, the charge
172 $Q_{cal} = V_{cal} \cdot (C_{inj1} + C_{inj2})$ is injected into the analog chain. Then the length of the
173 output pulse is measured and finally the feedback value is changed to either lengthen
174 or shorten the pulse in order to get to the required duration t_{cal} . The typical values
175 are $Q_{cal} = 5000 - 16000$ e at the time $t_{cal} = 5 - 10$ ToT. The target values depend
176 on the sensor, the type of a radioactive source and the application. Therefore the
177 initial threshold Th at 1 ToT and the calibrated value Q_{cal} at t_{cal} ToT give us a linear
178 scale of collected charge with respect to time over threshold. However, in practice

1.3. MODULE ASSEMBLY

179 this relation is nonlinear for lower thresholds, but since the goal of the measurements
180 is to track the particles rather than to measure their deposited energy precisely, this
181 is sufficient.

182 1.3 Module assembly

183 Parts for the detector arrived separately and were assembled into modules at CERN’s
184 DSF lab after being checked for production faults. The assembled modules underwent
185 a series of quality control (QC) and burn-in tests to determine their quality, efficiency
186 and long-term stability.

187 A DBM single-chip module consists of a hybrid pixel module, a flexible PCB and
188 the supporting mechanics (a ceramic plate and an aluminium plate). The chip arrives
189 already bump-bonded to the sensor, be it diamond or silicon. First it is glued to the
190 ceramic plate on one side and to the PCB on the other using Araldite 2011 or Staystik
191 672/472. Staystik is re-workable and has a very high thermal conductivity. The latter
192 is important because the FE-I4 chips tend to heat up significantly and need a good
193 heat sink. The problem is that it has a curing temperature of 160/170 °C. This
194 temperature may cause some unwanted stress build-up between the FE-I4 and the
195 diamond sensor due to different coefficients of thermal expansion, pulling them apart.
196 This would disconnect the pixels, yielding large regions of the module insensitive to
197 radiation. Araldite 2011 on the other hand can be cured at lower temperatures –
198 down to RT – but it has a lower heat conductivity. In the end Araldite is used as
199 a safer option. However, due to the longer curing, the entire assembly process using
200 Araldite is extended to two working days. After curing, the module is wire-bonded and
201 attached to the aluminium plate using screws made up of a radiation-resistant PEEK
202 plastic. They have to be tightened with a great care, because their screw head is only
203 0.2–0.6 mm away from the sensor edge – the sensor displacement tolerance during
204 gluing is of the order of 0.5 mm. Finally, the module is put in an aluminium carrier
205 which protects it from mechanical damage or electrostatic discharges. Figure 1.5
206 shows an assembled module.

207 1.4 Performance results

208 This section gives an overview of the performance results of the DBM modules
209 achieved during the QC and the test beam campaign. The source tests were per-
210 formed to check for disconnected regions in the sensors and to measure the diamond’s
211 efficiency. Only the modules with minimal disconnected regions and maximum effi-
212 ciency were chosen for installation.

213 1.4.1 Source test results

214 The modules are tested in the lab using an Reconfiguration Cluster Element readout
215 system [5] and a moving stage with two degrees of freedom. They are placed onto the

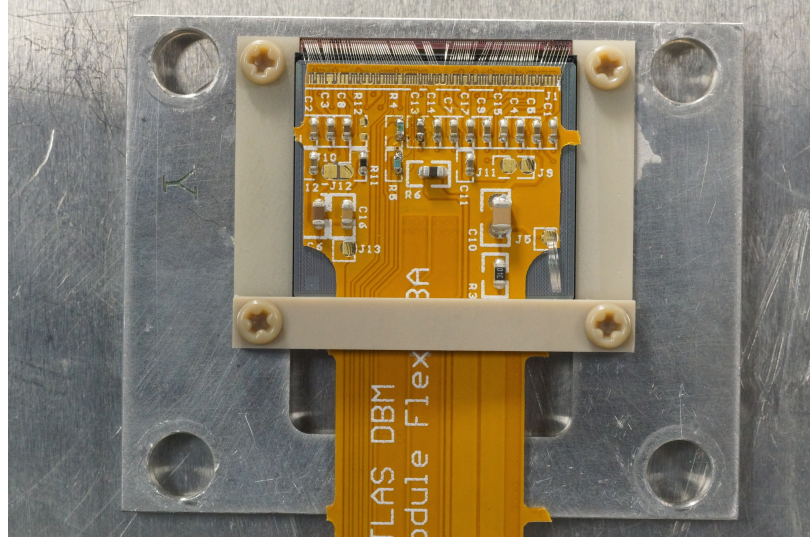


Figure 1.5: DBM module, top-down view. Visible is the flexible PCB with signal and power connections, the silicon sensor and a part of the FE-I4. Wire bonds from the PCB to the FE-I4 and to the sensor are also visible.

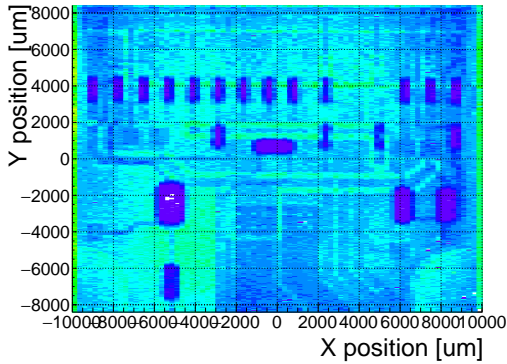
stage and connected to the readout system and the power supplies. After ensuring the low- and high voltage connectivity they are checked for the signal connectivity. If everything is operational, a series of automated tests is run. Each of these tests calibrates a certain value within a pixel, whether it is the signal threshold or the value for integrated charge. These are tuned in a way that the response to a predefined calibration signal is uniform for all pixels across the sensor. This procedure is referred to as *tuning*.

When the modules are tuned, they are tested using a ^{90}Sr radioactive source. Two characteristics of each module are checked: 1) operation of all pixels and 2) sensor efficiency.

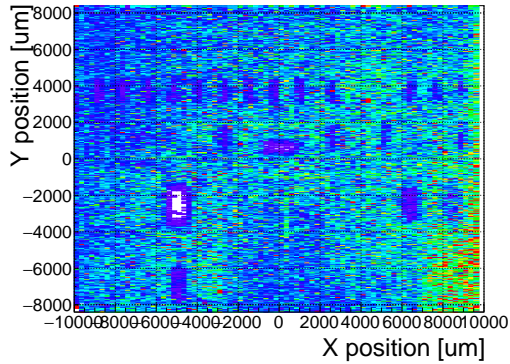
Pixel connectivity

The first test is carried out to determine the number of disconnected pixels in the matrix. This is an important step in the DBM QC procedure, because it turns out that a significant portion of the flip-chipped diamond sensors exhibited very poor connectivity. The disconnected regions on the faulty modules ranged anywhere from 0.5–80 % of the overall active surface. In two cases the sensor was even completely detached from the chip. Therefore the pixel connectivity turns out to be the most important qualification factor in the QC procedure. Unfortunately the only way to check it at the moment is to fully assemble a module and test it using a radioactive source. If the module turns out to be of poor quality, it is disassembled and sent for rework. The turnover time of this operation is of the order of one month, which affected the DBM installation schedule significantly. In the end the modules with less than 3 % disconnected pixels have been accepted.

1.4. PERFORMANCE RESULTS



(a) Occupancy scan for MSBM-34.



(b) Occupancy scan for MDBM-23.

Figure 1.6: Occupancy scans for the silicon (left) and diamond sensor (right) to check for disconnected regions. Shadows of the electronic components are clearly visible because fewer electrons were able to traverse through such a higher amount of material.

The test for disconnected regions is carried out by moving the module under the source in X and Y direction so that the exposure over the entire plane is uniform. The resulting occupancy map reveals pixels that are not electrically coupled to the sensor via bump bonds. The occupancy scans are shown in figures 1.6a and 1.6b. The silicon module has a very uniform occupancy plot. So much so that the features of the overlaying flexible PCB can be observed. The rectangular shadows are the passive components whereas the lines are the traces in the PCB. Furthermore, a circular-shaped edge of the PCB can be seen on the bottom right side of the plot. These darker areas are such because fewer electrons can penetrate the material with a high density. In the case of the diamond, the features of the PCB can be observed as well, but are much less distinguishable as the plot is much more granulated – less uniform. This high variance in the diamond’s detection ability is due to the grain boundaries in the pCVD material which trap the drifting charges, rendering some regions significantly less efficient.

Figure 1.7 shows the distribution of disconnected regions across all tested modules. Silicon modules were performing as expected, with a minimum number of disconnected pixels.

256 Pseudo-efficiency

Only the modules that passed the pixel connectivity test undergo the second test stage in which the sensor’s efficiency is estimated. A scintillator is placed underneath the module and is used as a trigger. A particle that crosses the DBM module and hits the scintillator, triggers the module readout. In the end, the number of triggers is compared to the number of hits/clusters recorded by the module. These are shown in figures 1.8a and 1.8b.

However, the resulting ratio is only an estimate of the sensor’s detection efficiency.

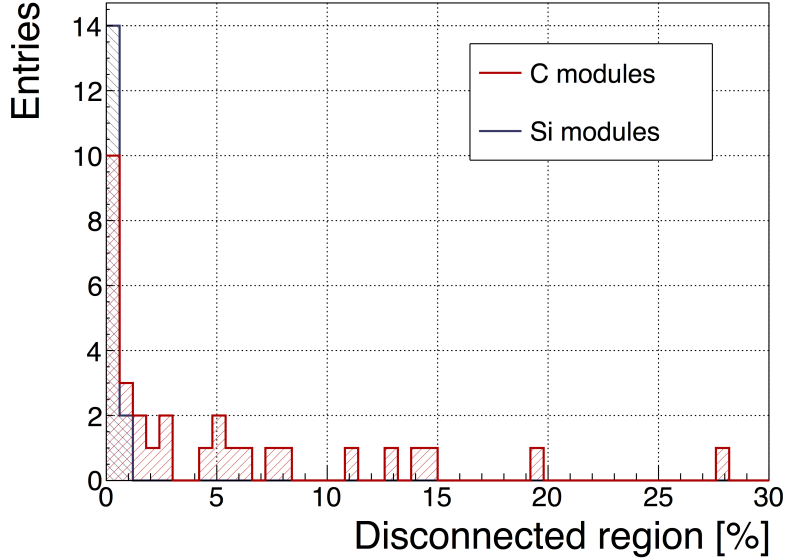


Figure 1.7: Disconnected regions for all modules derived from the occupancy scans.

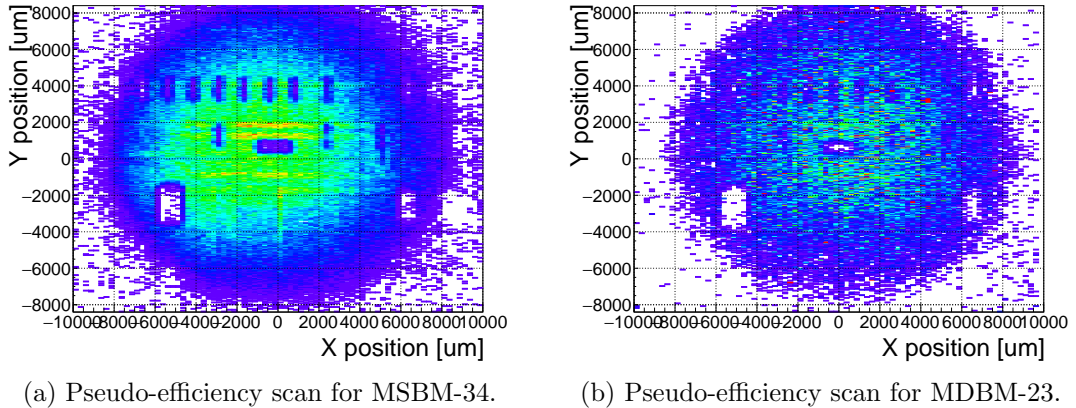


Figure 1.8: Pseudo-efficiency scans for the silicon (left) and diamond sensor (right) to estimate the efficiency of the sensors.

This is because the β particles scatter around the setup and sometimes hit the scintillator from other directions without traversing the module, producing empty triggers. Therefore the real sensor efficiency can only be measured in a high energy particle beam and using a beam telescope as a reference detector to measure the particle trajectories. Nonetheless, this *pseudo-efficiency* gives a rough estimate of the sensor's quality.

Figure 1.9 shows the distribution of pseudo-efficiencies for all modules that went through the QC. The majority of the silicon modules yield the pseudo-efficiency of (94.3 ± 0.2) %. Silicon sensors being 99.99 % efficient, this value is underestimated by about 5 %. The measured pseudo-efficiency of the diamond modules is (65 ± 7) %, with outliers down to 10 %. The value depends on the diamond quality, the set

1.4. PERFORMANCE RESULTS

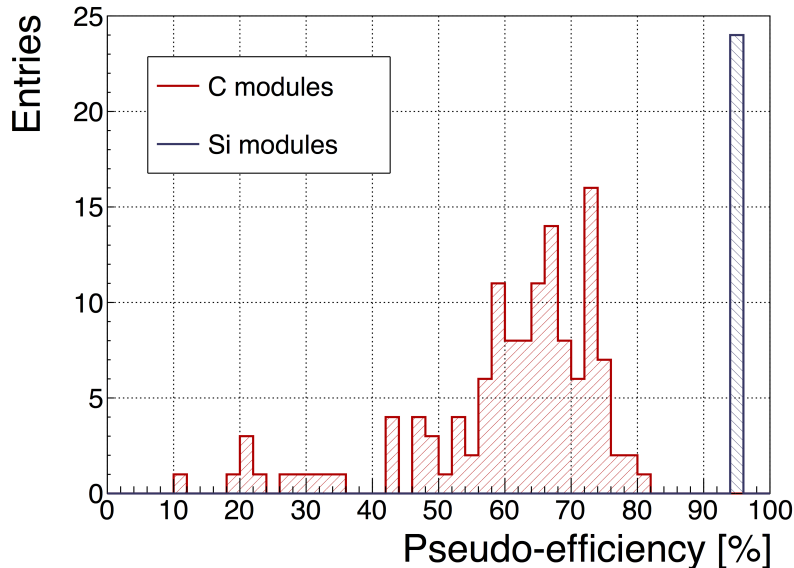


Figure 1.9: Pseudo-efficiencies for all modules at various threshold and voltage settings.

threshold and the applied bias voltage. The latter two settings are varied to check the behaviour of the modules under various conditions.

1.4.2 Erratic current

A very important parameter for qualifying a module is the erratic current [9] in the sensor. This term describes the leakage current in a pCVD diamond that becomes unstable. It can develop gradually or can be triggered with a β source. Spikes appear in the otherwise stable leakage current. They can be up to three orders of magnitude higher than the base current. Sometimes the current also suddenly increases for a few orders of magnitude and stays at that level (e.g. from the initial 1 nA to 3 μ A). An example of such behaviour is shown in figure 1.10.

The amplitude differs in magnitude from sensor to sensor. This effect is still not fully explained, but the hypothesis is that the charges find a conductive channel along the grain boundaries, causing discharges. These discharges are picked up by the pixel amplifiers in the FE-I4. A single discharge can trigger a group of up to \sim 500 pixels, resulting in a *blob* on the detector occupancy map. Sometimes the conductive channel stays in a conductive state, making one or more pixels always to fire. These pixels saturate the bandwidth of the readout channel, so they have to be masked out during measurements.

1.4.3 Test beam results

The first two assembled prototype DBM modules, MDBM-01 and MDBM-03, were tested at DESY, Hamburg, in a test beam facility. The aim of the measurements was

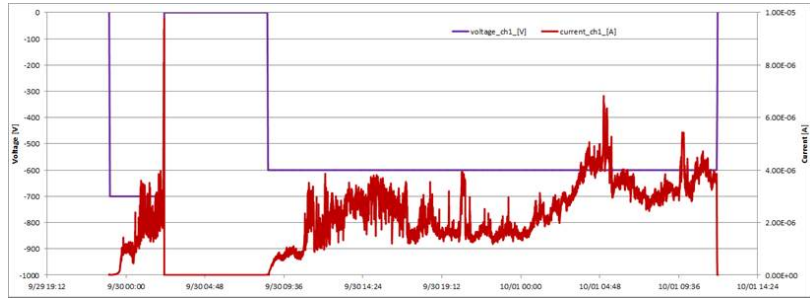


Figure 1.10: Erratic current in a DBM diamond module.

296 to measure their efficiency, the spatial distribution of the efficiency and the effect of
 297 the beam on the disconnected regions. A silicon module MSBM-02 was measured
 298 to crosscheck the measurements. Since the silicon module is almost 100 % efficient,
 299 it was used as an “anchor” – the efficiency of the diamond module was measured
 300 relative to that of the silicon module. Two beam telescopes were used as reference
 301 systems: Kartel telescope [8] built by JSI institute from Ljubljana, and EUDET
 302 Aconite [2]. Both are instrumented with six Mimosa26 pixel planes and capable of
 303 tracking particles with a 2 μm pointing resolution.

304 The test beam prototypes did not meet the acceptance criteria for production
 305 DBM modules in the following areas: first, the stated CCDs were slightly below
 306 200 μm , which would be the DBM minimum. Secondly, the applied bias voltages
 307 ranged from 1–2 V/ μm . In addition, the threshold cut could only be set to 1500 elec-
 308 trons, which is higher than the DBM minimum (1000 e). Nonetheless, the resulting
 309 module efficiencies were still in the range between 70–85 %.

310 To analyse the test beam data, Judith software framework [8] was used. Judith is
 311 capable of synchronising data streams from several detector systems only connected
 312 via a trigger system, reconstructing tracks and calculating efficiency for the DUTs. It
 313 was also used to reconstruct and analyse the acquired Kartel test beam data together
 314 with the silicon and diamond module as DUTs. A sample of the analysed data is
 315 shown in figures 1.11a and 1.11b.

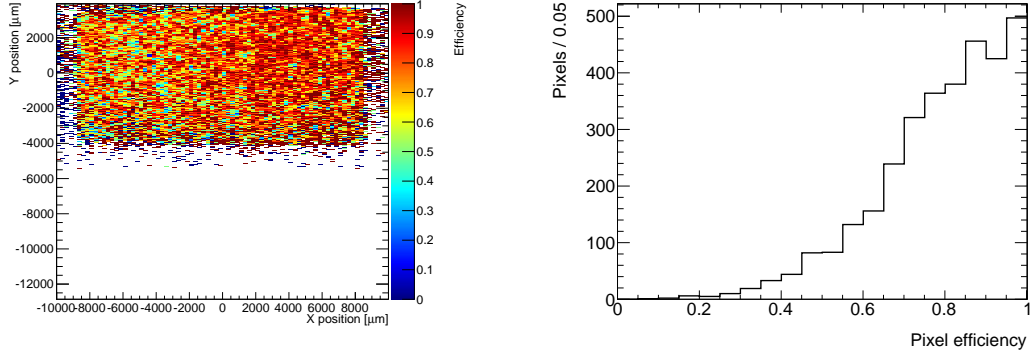
316 1.4.4 Summary of the QC

317 The results for the DBM QC are shown in section ???. All in all, 79 modules went
 318 through the QC procedure – 43 diamond modules and 36 silicon modules, 12 of the
 319 latter only for testing purposes. Figure 1.12 shows their production with time. 18
 320 diamond modules and 6 silicon modules were in the end chosen to be integrated into
 321 DBM telescopes and installed into ATLAS.

322 1.5 Installation and commissioning

323 The DBM modules that passed the QC tests were assembled into telescopes – sets
 324 of three modules one behind the other with a spacing of 50 mm. Of the 18 diamond

1.5. INSTALLATION AND COMMISSIONING



(a) This figure shows an efficiency map of a DBM pVCD diamond module. Each bin corresponds to a single pixel. The triggering scintillator of the Kartel telescope is smaller than the DUT. Hence, the recorded hits can only be seen in the top half of the sensor.

(b) A pixel efficiency distribution from the run in figure (a).

Figure 1.11: An efficiency study of a prototype DBM diamond module in a test beam. The statistics are low (~ 10 hits/pixel) as the data were collected during a short run.

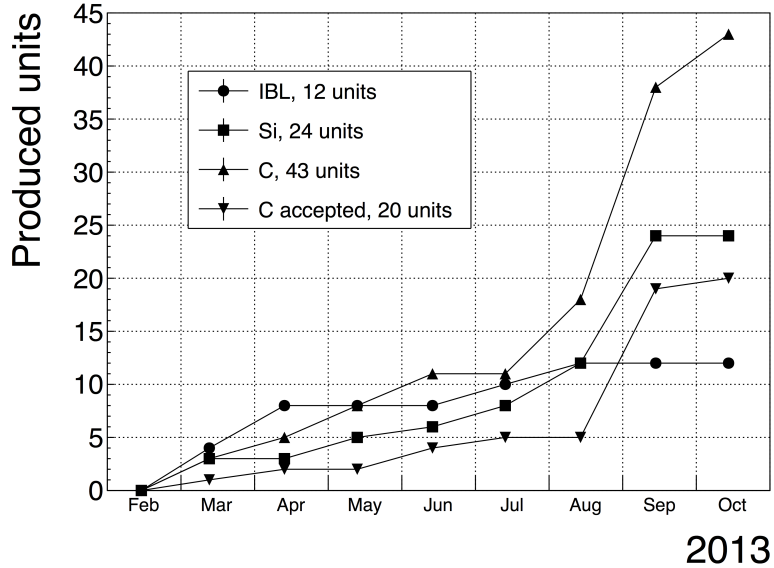


Figure 1.12: Module production with time.

and 6 silicon modules, 6 diamond and 2 silicon telescopes were built. A special care was taken when choosing the sets of three diamonds. The modules with a similar pseudo-efficiency, leakage current, maximum stable high voltage and shape of disconnected regions were grouped together. After assembly into telescopes, the modules were tested for their connectivity. Then the high voltage was applied and the leakage current was observed. This was an important point to check because all three modules shared the same high voltage channel. Any instabilities on one of the

332 modules would cause problems on the other two. This would for instance happen if
333 one of the modules had a much lower breakdown voltage.

334 Due to time constraints, the telescopes were not built at the same time but in-
335 stead the production was pipelined. As soon as two telescopes were ready, they were
336 transported to Point 1 – the site where parts of the ATLAS detector were being put
337 together. There they were prepared for installation onto the pixel detector struc-
338 ture that had been extracted from ATLAS due to pixel detector commissioning. The
339 commissioning was nearing completion, so the technicians were preparing the detec-
340 tor for re-insertion. The cylindrical structure was being enclosed by four new service
341 quarter-panels (nSQPs). This meant that with every day the access to the place
342 of installation of the DBM was more difficult. The first two telescopes were still put
343 into place when only one nSQP was in place. This allowed the installation process
344 to be carried out from both sides. This proved to be helpful, because the process
345 was lengthy and had to be done with great precision. It involved tightening several
346 screws on both sides of the telescopes, adding thermal paste on the aluminium joints
347 and removing the protective covers, revealing the fragile wire bonds. At the same
348 time the surrounding electronics and cables had to be left untouched. The lessons
349 learnt with the first part of the installation were helpful when installing the other tele-
350 scopes. The last two were fitted onto the structure when three nSQPs were already
351 in place, leaving only a narrow opening for access. The entire procedure was carried
352 out blind. After every installation, the telescopes were tested again. First, the low
353 voltage connectivity was checked and a set of tests was run on the FE-I4 front-end
354 chips. An eye diagram was made to estimate the quality of the signal transmission.
355 Then a ^{90}Sr source was used to perform a source test on three modules at the same
356 time. Leakage current was observed during the source test. The final test included
357 running four telescopes (all on one side) at a time. All the tests were successful and
358 the DBM was signed off.

359 **1.5.1 Positioning in ATLAS**

360 The DBM is placed in the forward region of the ATLAS detector very close to the
361 beam pipe, as shown in figure 1.14. Eight DBM telescopes reside approximately 1 m
362 away from the collision region, four on each side. They are tilted with respect to
363 the beam pipe for 10° . This is due to a specific phenomenon connected to erratic
364 (dark) currents in diamond. Studies have shown [9] that the erratic leakage currents
365 that gradually develop in diamond can be suppressed under certain conditions. For
366 instance, if a strong magnetic field is applied perpendicular to the electric field lines
367 in the diamond bulk, the leakage current stabilises. The DBM was designed to exploit
368 this phenomenon. The magnetic field lines in the ATLAS experiment are parallel to
369 the beam. Hence, an angular displacement of the sensor with respect to the beam
370 allows for the leakage current suppression. However, the DBM telescopes still need to
371 be directed towards the interaction region. Taking these considerations into account,
372 a 10° angle with respect to the beam pipe was chosen. The influence of the magnetic

1.6. OPERATION



Figure 1.13: This photo highlights four telescopes installed onto the nSQPs and around the pipe.

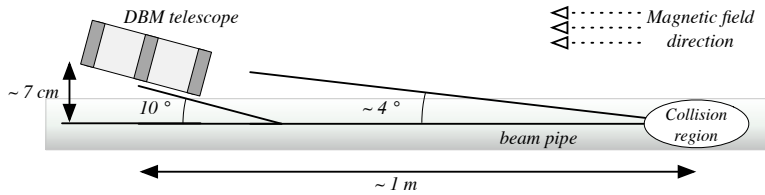


Figure 1.14: Position of the DBM in the ATLAS experiment.

373 field on the particle tracks at this angle is very low as the field lines are almost
374 parallel to the tracks. The tracks are therefore straight, which reduces the track
375 reconstruction complexity.

376 1.6 Operation

377 The DBM has been commissioned in ATLAS and is now taking data. Several issues
378 still need to be resolved regarding the readout system. Unfortunately, due to issues
379 with the low voltage power supply regulators, six out of 24 modules were damaged
380 during operation: four silicon and two diamond modules. The system configured
381 the modules into an unsteady state whereby they drew twice as much current as the
382 allowed maximum. This current most probably fused the wire bonds within minutes.
383 This has left only five diamond telescopes fully operational. The preliminary data
384 obtained using the remaining telescopes show that the background rejection could
385 indeed work.

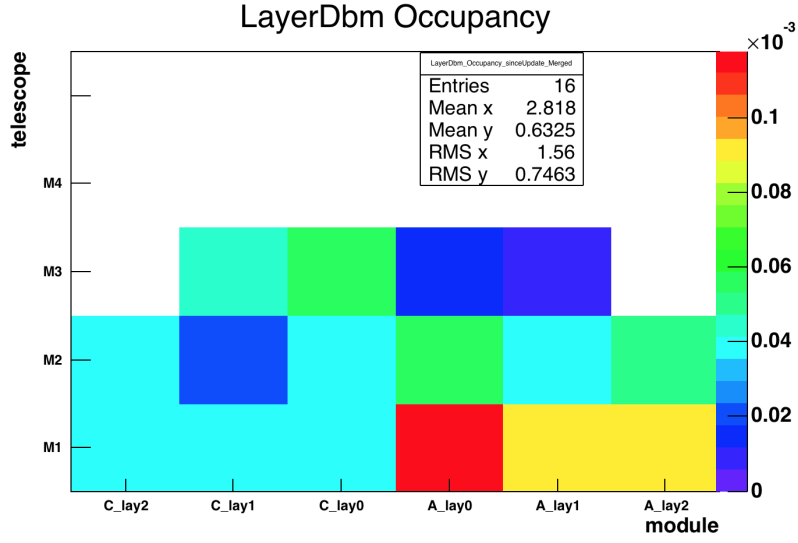


Figure 1.15: Occupancy of individual modules during collisions. Only 16 modules were taking data.

386 The first step of the system test was to take data during collisions and check
 387 the occupancy in the individual modules. The occupancies were plotted side by side
 388 for comparison. Figure 1.15 shows some of the occupancy values. At the time, the
 389 readout system was not yet configured to read out all telescopes in parallel.

390 The second step was to test the detector's capability of particle tracking. Only one
 391 telescope was used to take data with the beam. If all three planes of the telescope
 392 were hit during a bunch crossing, a linear line was fitted to the hits. This line
 393 represented the particle's trajectory. It was projected towards the interaction point.
 394 Two parameters were calculated where the line is the closest to the interaction point:
 395 the radial distance and the longitudinal distance between the line and the interaction
 396 point, as shown in figure 1.16. This was done for the events with two colliding bunches
 397 as well as for events with only one, non-colliding bunch. The tracks recorded during
 398 the events with two colliding bunches could either come from the collisions or could
 399 be background scattering. Tracks recorded during a non-colliding bunch, on the
 400 other hand, are definitely background particles since there are no collisions taking
 401 place.

402 A comparison of the data acquired and depicted in figures 1.17a and 1.17b shows
 403 that, for the colliding bunches, the majority of the reconstructed tracks had the origin
 404 in the interaction point, with a narrow spread in Z and R . For non-colliding bunches,
 405 the spread is wider. In the Z_0 plot the distribution has one peak in the middle, which
 406 means that the empty RF buckets still held some particles which collided. The two
 407 peaks on the sides, however, show that a significant number of tracks had their origin
 408 at the radius of the beam pipe. Therefore these tracks were made by stray protons
 409 colliding with the beam pipe. These collisions are unwanted as they do not produce
 410 any meaningful physics while still damaging the ATLAS detector by means of the

1.7. CONCLUSION

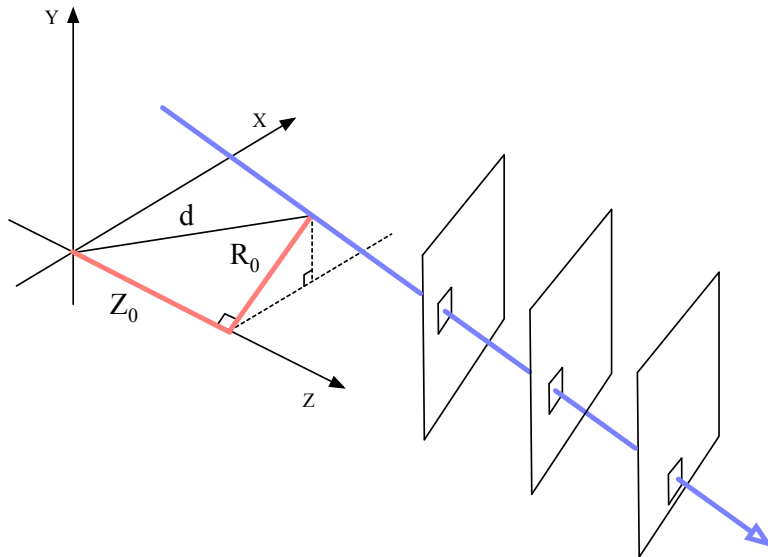


Figure 1.16: A diagram showing the radial distance R_0 and longitudinal distance Z_0 of the trajectory from the interaction point at the minimal distance d . Z is the axis along the beam line. Three module planes intercept a particle and reconstruct its trajectory.

411 scattered radiation.

412 1.7 Conclusion

413 The Diamond Beam Monitor has been designed as an upgrade to the existing lu-
414 minosity detectors in the ATLAS experiment. It is the first diamond pixel tracking
415 detector installed in a high-energy physics experiment. The pixelated front-end elec-
416 tronic chips ensure precise spatial detection of the charged high-energy particles.
417 The projective geometry allows for particle tracking and background rejection. The
418 detector is placed in a high-radiation forward region of the experiment. Therefore,
419 radiation hardness of the chosen pCVD diamond sensors is an important requirement.
420 The tests carried out in the test beam and in the laboratory confirmed that enough
421 detector-grade DBM modules have been built to be installed in the experiment. The
422 DBM is now running in ATLAS during collisions. Further improvements have to be
423 made on the readout firmware before it is included in the main readout stream.

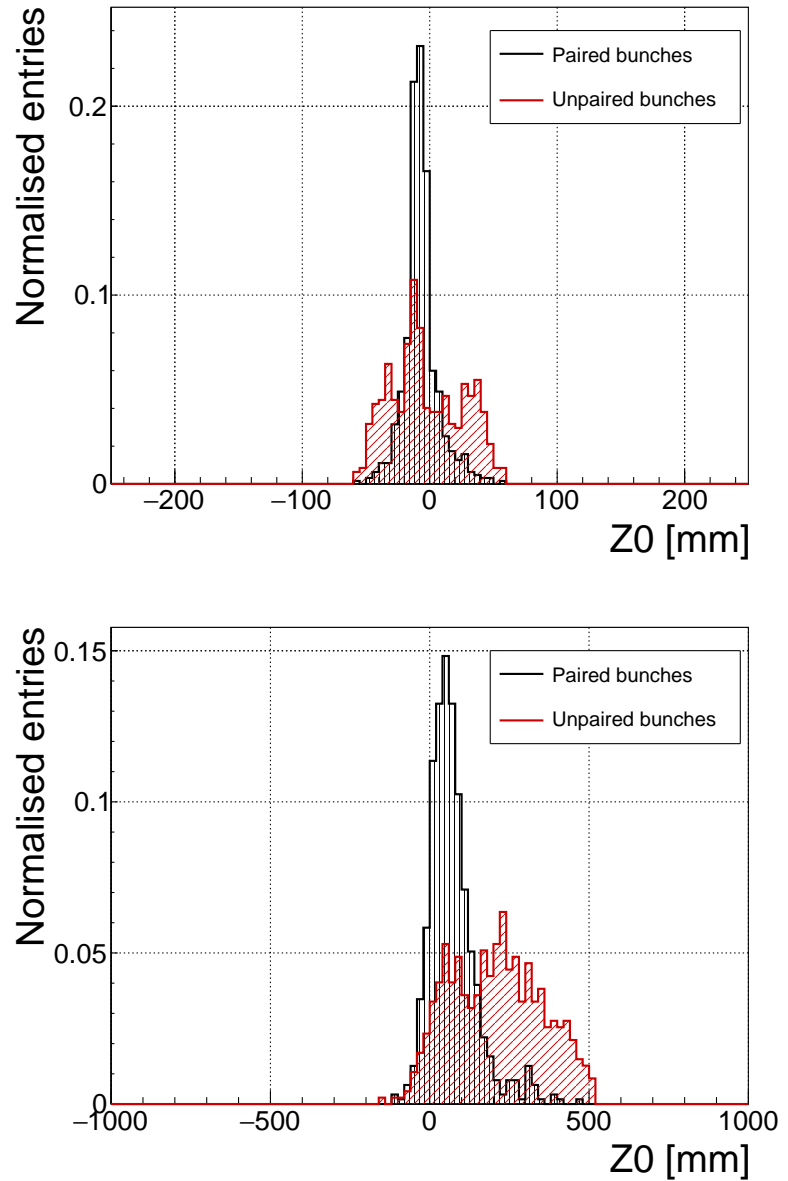


Figure 1.17: These two plots show two parameters of particle tracks recorded by one of the DBM telescopes: radial (a) and longitudinal (b) distance of the projected tracks from the interaction point.

₄₂₄

Bibliography

- ₄₂₅ [1] *CiS Forschungsinstitut fuer Mikrosensorik GmbH.* <http://www.cismst.org/>.
- ₄₂₆ [2] *EUDET ACONITE telescope.*
- ₄₂₇ [3] *Measurement of the Rate of Collisions from Satellite Bunches for the April-May*
₄₂₈ *2010 LHC Luminosity Calibration.* Technical Report ATLAS-CONF-2010-102,
₄₂₉ CERN, Geneva, Dec 2010.
- ₄₃₀ [4] J et al. Albert. *Prototype ATLAS IBL Modules using the FE-I4A Front-End*
₄₃₁ *Readout Chip.* *J. Instrum.*, 7(arXiv:1209.1906):P11010. 45 p, Sep 2012. Comments:
45 pages, 30 figures, submitted to JINST.
- ₄₃₃ [5] Richard Claus. *A New ATLAS Muon CSC Readout System with System on Chip*
₄₃₄ *Technology on ATCA Platform.* Jun 2015.
- ₄₃₅ [6] A Gorišek, V Cindro, I Dolenc, H Frais-Klbl, E Griesmayer, H Kagan, S Korpar,
₄₃₆ G Kramberger, I Mandic, M Meyer, M Mikuz, H Pernegger, S Smith, W Trischuk,
₄₃₇ P Weilhammer, and M Zavrtanik. *ATLAS diamond Beam Condition Monitor.*
₄₃₈ *Nucl. Instrum. Methods Phys. Res., A*, 572(1):67–69, 2007.
- ₄₃₉ [7] Fabian Huegging. *The ATLAS Pixel Insertable B-Layer (IBL).* *Nucl. Instrum.*
₄₄₀ *Methods Phys. Res., A*, 650(arXiv:1012.2742):45–49. 7 p, Dec 2010. Comments:
7 pages, 5 figures, 4 tables, accepted by Nuclear Instruments and Methods A for
442 publication.
- ₄₄₃ [8] Garrin McGoldrick, Matevž Červ, and Andrej Gorišek. *Synchronized analysis of*
₄₄₄ *testbeam data with the Judith software.* *Nucl. Instrum. Methods Phys. Res., A*,
₄₄₅ 765:140–145, 2014.
- ₄₄₆ [9] S Mueller, W deBoer, M Schneider, A Sabellek, M Schmanau, C Ruehle,
₄₄₇ T Schneider, and R Hall-Wilton. *Study of leakage currents in pCVD*
₄₄₈ *diamonds as function of the magnetic field.* *Phys. Status Solidi, A*,
₄₄₉ 206(arXiv:0905.0403):2091–2097. 6 p, May 2009. Comments: 6 pages, 16 fig-
₄₅₀ ures, poster at Hasselt Diamond Workshop, Mar 2009.
- ₄₅₁ [10] Matevž Červ. *The ATLAS Diamond Beam Monitor.* Technical Report ATL-
₄₅₂ INDET-PROC-2013-021, CERN, Geneva, Nov 2013.